Measurement of the ^{151}Sm(n, γ) cross section from 0.6 eV to 1 MeV via the neutron time-of-flight technique at the CERN n_TOF facility

S. Marrone,[16,*] U. Abbondanno,[19] G. Aerts,[9] F. Alvarez-Velarde,[26] H. Alvarez-Pol,[30] S. Andriamonje,[9] J. Andrzejewski,[21] G. Badurek,[1] P. Baumann,[7] F. Bečvář,[37] J. Benlliure,[30] E. Berthomieux,[9] F. Calviño,[31] D. Cano-Ott,[26] R. Capote,[4,29] P. Cennini,[32] V. Chepel,[22] E. Chiaveri,[32] N. Colonna,[16] G. Cortes,[31] D. Cortina,[30] A. Couture,[36] J. Cox,[36] S. Dababneh,[11] M. Dahlfors,[32] S. David,[6] R. Dolfini,[20] C. Domingo-Pardo,[27] I. Duran-Escribano,[30] M. Embid-Segura,[26] L. Ferrant,[6] A. Ferrari,[32] R. Ferreira-Marques,[22] H. Frais-Koelbl,[3] K. Fujii,[19] W. I. Furman,[24] R. Gallino,[18] I. F. Goncalves,[23] E. Gonzalez-Romero,[26] A. Goverdovski,[25] F. Gramegna,[15] E. Griesmayer,[3] F. Gunsing,[9] B. Haas,[8] R. Haight,[34] M. Heil,[11] A. Herrera-Martinez,[32] S. Isaev,[6] E. Jericha,[1] F. Käppeler,[11] Y. Kadi,[32] D. Karadimos,[12] M. Kerveno,[7] V. Ketlerov,[25] P. E. Koehler,[35] V. Konovalov,[25] M. Kritĉka,[37] C. Lamboudis,[13] H. Leeb,[1] A. Lindote,[22] M. I. Lopes,[22] M. Lozano,[29] S. Lukic,[7] J. Marganiec,[21] J. Martinez-Val,[28] P. F. Mastinu,[15] A. Mengoni,[4,32] P. M. Milazzo,[19] A. Molina-Coballes,[29] C. Moreau,[19] M. Mosconi,[11] F. Neves,[22] H. Oberhummer,[1] S. O'Brien,[36] J. Pancin,[9] T. Papaevangelou,[32] C. Paradela,[30] A. Pavlik,[2] P. Pavlopoulos,[10] J. M. Perlado,[28] L. Perrot,[9] M. Pignatari,[18] M. T. Pigni,[1] R. Plag,[11] A. Plompen,[5] A. Plukis,[9] A. Poch,[31] A. Policarpo,[22] C. Pretel,[31] J. M. Quesada,[29] S. Raman,[35,†] W. Rapp,[11] T. Rauscher,[33] R. Reifarth,[34] M. Rosetti,[14] C. Rubbia,[20] G. Rudolf,[7] P. Rullhusen,[5] J. Salgado,[23] J. C. Soares,[23] C. Stephan,[6] G. Tagliente,[16] J. L. Tain,[27] L. Tassan-Got,[6] L. M. N. Tavora,[23] R. Terlizzi,[16] G. Vannini,[17] P. Vaz,[23] A. Ventura,[14] D. Villamarin-Fernandez,[26] M. Vincente-Vincente,[26] V. Vlachoudis,[32] F. Voss,[11] H. Wendler,[32] M. Wiescher,[36] and K. Wisshak[11]

(n_TOF Collaboration)

[1]*Atominstitut der Österreichischen Universitäten, Technische Universität Wien, Austria*
[2]*Institut für Isotopenforschung und Kernphysik, Universität Wien, Austria*
[3]*Fachhochschule Wiener Neustadt, Wien, Austria*
[4]*International Atomic Energy Agency, NAPC-Nuclear Data Section, Wien, Austria*
[5]*CEC-JRC-IRMM, Geel, Belgium*
[6]*Centre National de la Recherche Scientifique/IN2P3-IPN, Orsay, France*
[7]*Centre National de la Recherche Scientifique/IN2P3-IreS, Strasbourg, France*
[8]*Centre National de la Recherche Scientifique/IN2P3-CENBG, Bordeaux, France*
[9]*CEA/Saclay-DSM/DAPNIA/SPhN, Gif-sur-Yvette, France*
[10]*Pôle Universitaire Léonard de Vinci, Paris La Défense, France*
[11]*Forschungszentrum Karlsruhe GmbH, Institut für Kernphysik, Germany*
[12]*University of Ioannina, Ioannina, Greece*
[13]*Aristotle University of Thessaloniki, Thessaloniki, Greece*
[14]*ENEA, Bologna, Italy*
[15]*Instituto Nazionale di Fisica Nucleare, Laboratori Nazionali di Legnaro, Italy*
[16]*Dipartimento di Fisica and INFN Bari, Italy*
[17]*Dipartimento di Fisica and INFN Bologna, Italy*
[18]*Dipartimento di Fisica Generale and INFN Torino, Italy*
[19]*Instituto Nazionale di Fisica Nucleare Sezione di Trieste, Italy*
[20]*Università degli Studi Pavia, Italy*
[21]*University of Lodz, Poland*
[22]*LIP-Coimbra and Departamento de Fisica da Universidade de Coimbra, Coimbra, Portugal*
[23]*Instituto Tecnológico e Nuclear, Lisboa, Portugal*
[24]*Joint Institute for Nuclear Research, Frank Laboratory of Neutron Physics, Dubna, Russia*
[25]*Institute of Physics and Power Engineering, Obninsk, Russia*
[26]*Centro de Investigaciones Energéticas Medioambientales y Tecnologicas, Madrid, Spain*
[27]*Consejo Superior de Investigaciones Científicas, University of Valencia, Valencia, Spain*
[28]*Universidad Politécnica de Madrid, Spain*
[29]*Universidad de Sevilla, Spain*
[30]*Universidade de Santiago de Compostela, Spain*
[31]*Universitat Politècnica de Catalunya, Barcelona, Spain*
[32]*CERN, Geneva, Switzerland*
[33]*Department of Physics and Astronomy, University of Basel, Switzerland*
[34]*Los Alamos National Laboratory, Los Alamos, New Mexico, USA*
[35]*Oak Ridge National Laboratory, Physics Division, Oak Ridge, Tennessee, USA*
[36]*University of Notre Dame, Notre Dame, Indiana, USA*
[37]*Charles University, Prague, Czech Republic*

034604-1

The ^{151}Sm(n, γ) cross section was measured with the time-of-flight technique from 0.6 eV up to 1 MeV relative to the Au standard with an overall uncertainty of typically 6%. Neutrons were produced by spallation at the innovative n_TOF facility at CERN; the γ rays from capture events were detected with organic C_6D_6 scintillators. Experimental setup and data analysis procedures are described with emphasis on the corrections for detection efficiency, background subtraction, and neutron flux determination. At low energies, resonances could be resolved up to about 1 keV, yielding a resonance integral of 3575 ± 210 b, an average s-wave resonance spacing of $\langle D_0 \rangle = 1.49 \pm 0.07$ eV, and a neutron strength function of $\langle S_0 \rangle = (3.87 \pm 0.33) \times 10^{-4}$. Maxwellian-averaged capture cross sections are reported for thermal energies between 5 and 100 keV. These results are of relevance for nuclear structure studies, nuclear astrophysics, and nuclear technology. The new value of the Maxwellian-averaged cross section at $kT = 30$ keV is 3.08 ± 0.15 b, considerably larger than previous theoretical estimates, and provides better constraints for the thermodynamic conditions during the occurrence of the *slow* neutron capture process in low-mass stars during their asymptotic giant branch phase.

I. INTRODUCTION

Accurate knowledge of the ^{151}Sm(n, γ) cross section has important implications for fundamental nuclear physics, nuclear astrophysics, and nuclear technology. From the point of view of fundamental nuclear physics, the study of ^{152}Sm via the compound system $n + {}^{151}$Sm is of interest with respect to the role of nuclear structure in the rare-earth region. In fact, ^{152}Sm exhibits a high neutron separation energy of 8.258 MeV, a large average multiplicity (>4) of the de-excitation cascade, and a soft γ-ray spectrum. These features strongly characterize nuclear parameters such as the neutron strength function, the nuclear level density, and the γ-ray strength function. Comparison of these quantities with the other samarium isotopes (e.g., with the neutron magic ^{144}Sm and the deformed rotor ^{154}Sm) or with the neighboring Nd and Eu isotopes provides a crucial test for statistical and microscopic nuclear model calculations.

The ^{151}Sm(n, γ) cross section is also of great importance in nuclear astrophysics since ^{151}Sm is one of the main branch point isotopes in the *slow* neutron capture process (*s* process). As sketched in Fig. 1, the competition between neutron capture and β decay leads to a split of the reaction path at ^{151}Sm followed by a second branching at ^{154}Eu. Although the additional branch points ^{152,155}Eu and ^{153}Gd are of minor importance, the branchings at ^{151}Sm and ^{154}Eu determine the abundances of the s-only isotopes ^{152}Gd and ^{154}Gd, respectively. Since the β-decay rate of ^{151}Sm depends on temperature this branching can be used to extract important information on the thermodynamic conditions during the s process from the local abundance pattern in this mass range [1].

Finally, the fission product ^{151}Sm is abundantly produced in nuclear reactors. Although its half-life of 93 yr is relatively short compared to other long-lived fission products, it is included in advanced incineration schemes and, therefore, included in the Nuclear Energy Agency (NEA) High Priority Nuclear Data Request List [2]. Similar needs have been formulated in the United States and Japan [3] and are mainly

related to the development of new reactor concepts such as the Accelerator Driven Systems (ADS) [4], which are intrinsically safe and designed to incinerate radioactive wastes.

The radioactivity of ^{151}Sm represents a challenge in neutron capture measurements. The previous experimental data were derived long ago from transmission measurements by Pattenden [5] and by Kirouac and Eiland [6]. To improve this situation and to satisfy the various requests, a capture measurement has been performed at the innovative neutron time-of-flight facility (n_TOF) at CERN. The goal of the experimental program at n_TOF is to measure neutron capture and fission cross sections relevant to nuclear astrophysics, ADS, and related applications [7]. The characteristics of the facility [8,9] are perfectly suited for accurate measurements of (n, γ) cross sections over a wide energy range, including radioactive isotopes such as ^{151}Sm. In fact, the ^{151}Sm(n, γ) study was the very first measurement after the completion and commissioning of the n_TOF facility and represents a remarkable illustration of its unique performance.

The characteristics of the neutron beam and of the experimental apparatus are described in Sec. II. The data analysis procedures are outlined in Sec. III with emphasis on efficiency corrections, background subtraction, and neutron flux normalization. The results and the analysis of the related uncertainties in the resolved resonance region from 0.6 eV to 1 keV, and in the unresolved resonance region from 1 keV to 1 MeV, are illustrated in Sec. IV. Finally, the implications for fundamental nuclear physics, nuclear astrophysics, and nuclear technology are discussed in Sec. V.

II. EXPERIMENTAL SETUP

A. The n_TOF facility

The neutron beam at n_TOF is produced by spallation of a 20 GeV/c proton beam from the CERN proton synchrotron (PS) onto a massive natural Pb target. The main characteristics of the proton beam are summarized in Table I. The PS is delivering 7-ns-wide bunches of 7×10^{12} protons with a maximal repetition rate of 0.8 Hz, but presently only five bunches can be accepted within the PS supercycle of 14.4 s owing to limitations set by the cooling system. The high energy of the proton beam and the high proton intensities

---

*Corresponding author: INFN-Bari via Orabona 4, I-70126 Bari, Italy; e-mail: stefano.marrone@ba.infn.it
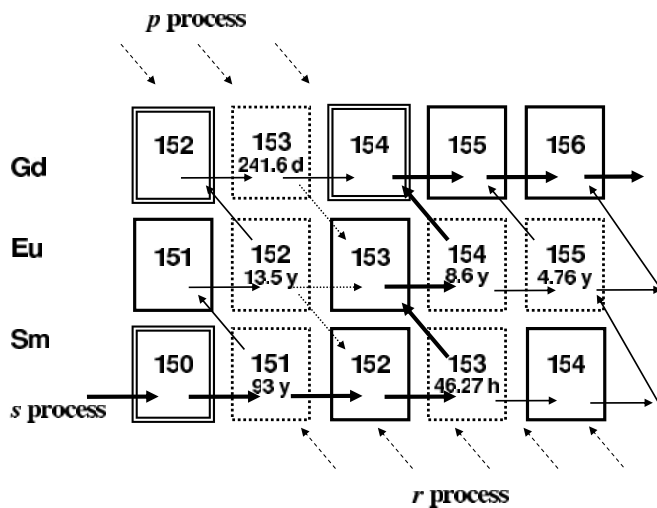
†Deceased.

FIG. 1. Reaction network illustrating the *s*-process branchings in the Sm-Eu-Gd region. Neutron capture, β decay, and electron capture are indicated by arrows. The *s*-only isotopes are marked by double boxes. Unstable isotopes are given with their terrestrial half-lives.

FIG. 2. Schematic sketch of the experimental setup used in the capture measurement.

in the bunches yield a high instantaneous neutron flux of $\sim 10^5$ per pulse and per energy decade at the experimental station 185 m from the target. The n_TOF neutron spectrum covers a wide energy range from thermal up to 250 MeV. A more detailed description of the technical features of the facility and its performance is given elsewhere [8,9]. The neutron beam profile is defined by two collimators in the evacuated flight path. For all capture cross section measurements, an aperture of 19 mm in diameter is used for the second collimator just upstream of the experimental area, resulting in an approximately Gaussian beam profile at the sample position with a FWHM of 11.75 mm [10]. A very low background level has been achieved in the experimental area owing to several massive concrete and iron shieldings and by means of a strong sweeping magnet. The start signal for the time-of-flight (TOF) measurement is accurately defined by the so-called prompt flash, resulting from ultrarelativistic particles such as electrons, muons, and γ rays produced by the impact of the PS proton pulse on the spallation target.

TABLE I. Main characteristics of the n_TOF facility.

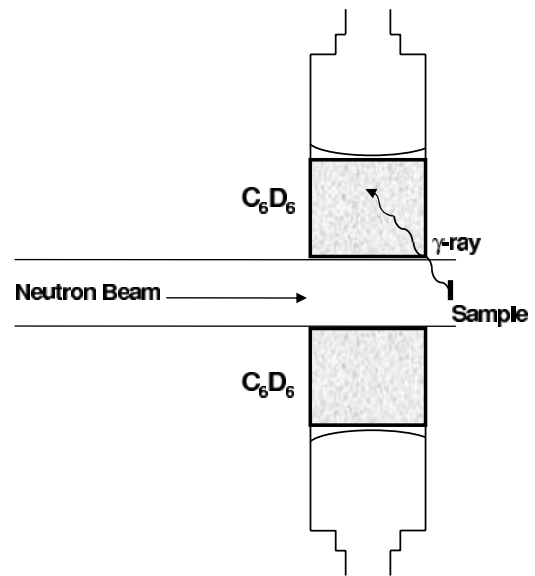|	
Proton beam	20 GeV/c momentum, pulse width 7 ns (rms), repetition frequency 0.4 Hz
	Intensity 7×10^{12} protons/pulse
Neutron beam	300 neutrons/proton generated in the spallation process, energies from 0.1 eV to 250 MeV
	Sweeping magnet, two collimators, and shielding walls for background reduction
	Neutron filters for background definition
	Neutron flux at 185 m, $\Phi \sim 10^5$ neutrons/ pulse/energy-decade
	Resolution in neutron energy, $\Delta E / E = 10^{-3}$ at 30 keV

B. Detectors

The setup for the capture measurements is schematically sketched in Fig. 2. It consists of a low-mass neutron flux monitoring system based on silicon detectors and two C_6D_6 scintillation detectors for the prompt capture γ rays.

The flux monitor consists of a Mylar foil 1.5 μm in thickness with a ^{6}Li layer of 200 μg/cm^2. The tritons and α particles from the ^{6}Li$(n, \alpha)^3$H reaction are recorded by a set of four silicon detectors outside the beam [11]. The whole system is mounted in a carbon-fiber scattering chamber located at the entrance of the experimental area 183 m from the spallation target. The silicon monitor (SiMon) is mainly used for the relative normalization of the spectra taken with the sample under investigation and the gold reference sample or the samples used for background determination such as carbon and lead.

The detection of neutron capture events is based on the prompt γ-ray cascade. The deuterated benzene (C_6D_6) liquid scintillators used in the present measurement consisted of cylindrical cells 127.3 mm in diameter and 78 mm in length with an active volume of ~ 1000 cm^3. Deuterated benzene was chosen for its very small neutron sensitivity. The neutron sensitivity of the detectors was further minimized by coupling a thin carbon-fiber cell directly to the EMI 9823QKA photomultipliers [12].

C. Data acquisition

The high instantaneous neutron flux at n_TOF is of great advantage, especially for the measurements of small radioactive samples. However, it represents a challenging problem for data acquisition and signal processing because of pileup and dead-time effects. These difficulties are solved by an innovative data-acquisition system based on fast digitizers, which records the full analog waveform of the detector

TABLE II. Characteristics of samples and of the experimental runs. All samples are enclosed in a Ti can and are 10 mm in diameter.

Sample	Chemical form	Mass (g)	Thickness (atoms/b)	Neutron filters (thickness in mm)	# of protons (units of 10^{17})
^{151}Sm	Sm_2O_3	0.20640	7.991×10^{-4}	none	1.64
^{197}Au	metal	1.48556	5.784×10^{-3}	none	0.36
^{nat}Ti can	metal	0.40104	6.022×10^{-3}	none	0.98
^{nat}C	powder	0.23602	1.496×10^{-2}	none	0.20
^{nat}Pb	metal	0.95745	3.543×10^{-3}	none	0.14
^{151}Sm	Sm_2O_3	0.20640	7.991×10^{-4}	Mo (1) + W (0.8) + Ag (0.5)	0.40
^{151}Sm	Sm_2O_3	0.20640	7.991×10^{-4}	Al (29.4)	0.32
					4.04

signal during the entire transit time of the neutron burst. The sampling is performed by means of flash analog to digital converters (FADCs) with maximal sampling rates of 10^9 s^{-1}. The raw data taken in this way consist of a series of signals, preceded and followed by a defined number of samples for baseline determination. These signals are analyzed off-line by determining the corresponding information on TOF, charge, amplitude, and particle type [13].

D. Samples

Table II lists all samples used in the measurement, their characteristics, and the number of protons used in the respective measurement and in the runs with black resonance filters in the neutron beam.

The ^{151}Sm sample consisted of 206 mg of Sm_2O_3 powder pressed to a solid pellet 10 mm in diameter. The sample was sealed inside a canning of natural titanium, consisting of a body 15 mm in diameter with a central depression for the sample pellet. The lid had a corresponding depression matching the sample thickness and was welded to the body at the outer circumference. The sample was chemically purified and prepared at the Oak Ridge National Laboratory (ORNL) 2.6 yr prior to the n_TOF measurement. Immediately after purification the isotopic composition listed in the second row of Table III was determined by mass spectrometry. At the time of the measurement the enrichment in ^{151}Sm was $\sim$88% with respect to the number of samarium and europium atoms and the decay product ^{151}Eu had grown to slightly more than 1.7% (third row of Table III). The total sample activity was 150 GBq. The ^{151}Eu impurity could be verified via the respective cross section resonances (Fig. 4). The isotopic composition of the sample was taken into account in the analysis of the capture

cross section. All other samples used in the measurement were also 10 mm in diameter and were enclosed in identical Ti cans to exhibit the same background contributions as measured with the ^{151}Sm sample.

The set of additional samples, which were all canned in the same way, included a gold disk since the capture cross section of ^{197}Au is used for the reference measurement, as reported in Sec. III C. An empty Ti can was used to determine the ambient background in the experimental area, which was common to all samples. The background caused by neutrons scattered from the sample and captured by the walls or by other materials in the experimental area was measured with a natural carbon sample. Although the capture cross section of carbon is negligible compared to the cross section for elastic scattering, the low atomic number ensures also a minimal contribution from the scattering of in-beam γ rays. In turn, the background caused by the interaction of in-beam γ rays was measured by means of a natural lead sample, as reported in Sec. III B.

III. DATA ANALYSIS

The main steps in data analysis are the application of the pulse height weighting technique (PHWT) for the efficiency correction, the identification and subtraction of backgrounds, the relative and absolute normalization, and the determination of the corrections for threshold effects, dead time, neutron multiple scattering, and isotopic impurities.

A. Pulse height weighting technique

As illustrated in Fig. 2, the two C_6D_6 detectors were positioned 90 mm upstream of the sample at 30 mm from the beam axis to reduce the contribution of scattered in-beam

TABLE III. Isotopic composition of the Sm_2O_3 sample. The second row reports the samarium isotopic composition present in Sm_2O_3 when the europium was separated in October 1999 (see Wisshak *et al.* [29] for details). The capture measurement in June 2002 indicates a sizable presence of ^{151}Eu. The third row reports the isotopic composition with respect to the initial number of samarium atoms and taking into account a ^{151}Sm half-life of 93 yr. Finally, the neutron separation energy (S_n) of each compound nucleus (n + relative isotope) is indicated in the last row.

	^{144}Sm	^{147}Sm	^{148}Sm	^{149}Sm	^{150}Sm	^{151}Sm	^{152}Sm	^{154}Sm	^{151}Eu	^{197}Au
Composition (%) (October 1999)	0.05	1.37	0.22	0.40	3.93	90.05	3.32	0.66	0.00	—
Composition (%) (June 2002)	0.05	1.37	0.22	0.40	3.93	88.28	3.32	0.66	1.77	99.99
S_n (MeV)	6.757	8.141	5.871	7.985	5.596	8.257	5.867	5.807	6.306	6.513

γ rays. The efficiency of the present setup is about 4% on average for γ rays in the energy range from 200 keV to 10 MeV. Since the efficiency for capture events depends on the characteristics of the de-excitation cascade, in particular on the γ-ray multiplicity, the PHWT had to be used. The PHWT original procedure was proposed long ago [14]. More recently, this technique has been updated and put on firm ground for the data analysis of several experiments at ORNL [15] and nowadays at n_TOF [16], where it has been validated by the study of the ^{197}Au, Ag, and ^{56}Fe standard resonances.

The γ-ray efficiency of the experimental setup was chosen sufficiently low so that at most one γ ray is detected for each capture cascade. The probability for detecting a capture event depends, therefore, on the γ-ray multiplicity of the cascade as well as on the energy of the emitted γ rays, since the intrinsic detector efficiency varies with γ-ray energy. These dependencies are compensated by the PHWT, which consists in a software modification of the response function $R(E_n, E_D)$ of the C_6D_6 detectors, where E_D is the energy deposited in the scintillator and E_n is the neutron energy. Multiplying the response function with an ad hoc weighting function $WF(E_D)$, which is chosen so that the detection efficiency for single γ rays becomes strictly proportional to their energy, one obtains an overall constant detection efficiency for capture events. The weighting functions for the various samples have been calculated on the basis of Monte Carlo simulations of the detector response, as described in detail in Ref. [16].

For the present analysis, simulations were performed with three different codes, GEANT-3 [17], GEANT-4 [18], and MCNP [19]. Application of the various weighting functions leads to differences of up to 4% in the extracted yields. These differences are reduced to less than 2% if the cross sections are determined relative to a reference sample (i.e., to gold) provided that the weighting functions are consistently calculated by using the same code for both samples. In this case, differences in the Monte Carlo simulations (geometrical details, tracking of the photons, etc.) affect both samples in a similar way.

The reliability of the PHWT is based on the assumption that only one γ ray per capture cascade is detected. This condition is ensured by the low overall efficiency of the detectors. Nevertheless, the probability for detecting coincident γ rays within the time window of 20 ns used in the present case is not completely negligible. Such events are overweighted and cause an artificial increase of the capture yield that has to be corrected for. Whereas coincident signals in both detectors can be easily identified and corrected by discarding one of the signals, absorption of two γ rays in the same detector produces a unique signal, but of larger amplitude. The effect of this contribution to the uncertainty has been derived from the measurement of the probability for coincidences in both detectors and was found to be $\sim$7%. The corresponding effect for the Au reference sample was only $\sim$4% owing the different multiplicity and energy distribution of its γ-ray cascade. The resulting net correction for the ^{151}Sm yield relative to Au amounts to 1.6% with a relative uncertainty of less than 0.5%.

Because of the characteristics of the FADC the dead time of the data acquisition system is zero. However, events separated by less than the coincidence window of 20 ns cannot be

distinguished from each other. A corresponding correction factor for the measured count rate was obtained as a function of TOF by means of the "paralyzable model" approximation, which accounts for the virtual dead time of 20 ns [20]. This correction exceeds the 1% level only above 10 keV and at the top of the main resonances.

The capture yield Y_{Raw}, is obtained according to the PHWT expression:

$$E_{\mathrm{casc}} \int \Phi(E'_n) Y_{\mathrm{Raw}}(E'_n) \, dE'_n = \sum_{E_D=0.2\,\mathrm{MeV}}^{10\,\mathrm{MeV}} R(E_n, E_D) WF(E_D),$$

(1)

where $\Phi(E_n)$ denotes the total neutron fluence impinging on the sample and E_{casc} the energy of the capture cascade converted to the laboratory frame. This yield has to be corrected for the different background components as well as for other effects such as Doppler broadening, self-shielding, multiple scattering, and neutron energy resolution.

B. Backgrounds

In general, capture measurements at n_TOF are affected by essentially three different sources of background [21]: neutrons scattered by the sample, in-beam γ rays, and the ambient background. The ambient background is mostly generated by particles from the spallation target, which have passed the shieldings and the sweeping magnet. This component is proportional to the intensity of the proton beam on target and hence to the total neutron fluence because the contribution from "true" ambient γ rays is negligible. In the present case, an additional component, common to all samples and proportional only to the integrated neutron fluence, is caused by the Ti cans of the samples. As illustrated in Fig. 3, this component is small in the entire energy range and can be easily subtracted.

The background related to neutrons scattered by the sample and captured in the walls of the experimental area, in the detectors, or in surrounding materials was investigated by means of a natural carbon sample that was chosen to match the elastic scattering effect of the Sm_2O_3 sample. The spectrum of the carbon sample was found to show no enhancement with respect to the spectrum of the empty Ti can. The effect of scattered neutrons was negligible because of the very low neutron sensitivity of the setup, and because materials with large capture cross sections had been completely removed from the experimental area. The use of carbon fiber for constructing the liquid scintillator cells, the entire sample changer, and the adjacent parts of the beam pipe was particularly important in this context.

A more severe background component is associated with in-beam γ rays scattered by the sample. This component was investigated by measuring a sample of natural lead. From the TOF spectrum of this lead sample, a sizable background for neutron energies above 1 keV can be inferred. Since photon scattering depends on characteristics of the samples (number of atoms and atomic number), Monte Carlo simulations have been performed to relate the TOF spectra and to determine
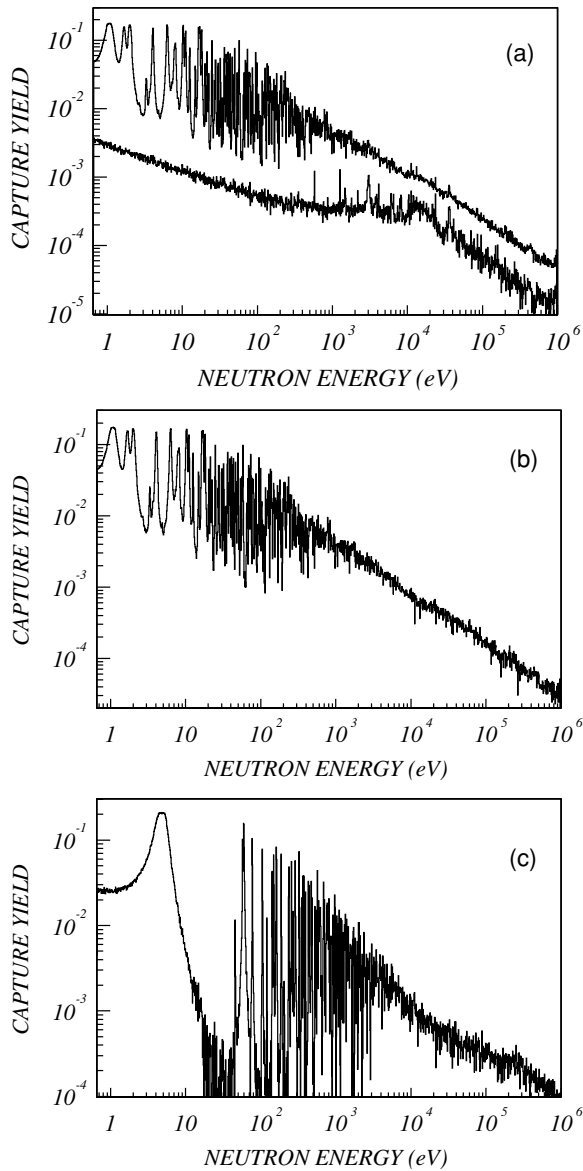
FIG. 3. Samarium capture yields (a) before and (b) after background subtraction. (c) Background-corrected Au yield. The spectrum of the Ti can in (a) exhibits the Ti resonances at 3, 8, and 13 keV.

the absolute value of the γ-ray background component for the samarium and gold samples. The energy spectrum of the incident in-beam γ rays was adopted from FLUKA [22] simulations of the spallation and moderation process of the n_TOF target module. The result of this investigation has been that the background from in-beam γ rays is one order of magnitude lower for the Sm_2O_3 sample than for the Pb sample and affects the measured ^{151}Sm yield only marginally. For gold, however, this background component is comparable to that of lead and was determined by scaling the measured spectrum of the Pb sample. Eventually, the background-subtracted capture yields

$$Y_{\mathrm{BS}}(E_n) = Y_{\mathrm{sample}}(E_n) - Y_{\mathrm{Ti\text{-}can}}(E_n)$$
$$- C_\gamma [Y_{\mathrm{Pb}}(E_n) - Y_{\mathrm{Ti\text{-}can}}(E_n)] \qquad (2)$$

TABLE IV. The probability C_γ for recording in-beam γ rays with energies above 200 keV with respect to the Pb sample.

Sample	Sm_2O_3	^{197}Au	^{nat}C	Ti can	^{nat}Pb
C_γ	0.128	1.55	1.95×10^{-2}	6.43×10^{-2}	1

were calculated for the ^{197}Au and the Sm_2O_3 samples. In this expression Y_{sample} denotes the raw capture yield measured for a given sample, $Y_{\mathrm{Ti\text{-}can}}$ is the yield measured with the empty Ti can, and Y_{Pb} is the yield measured with the Pb sample, all obtained with a consistent set of weighting functions. The third term in Eq. (2) represents the background contribution by in-beam γ rays. The measured Pb yield is adjusted by the scaling factor C_γ to account for the effect of in-beam γ rays scattered by the sample under consideration. Numerical values for C_γ, which were obtained by adopting a 200-keV threshold in γ-ray energy in the simulations, are listed in Table IV. Statistical fluctuations owing to the comparably small background yield and the weak effect of Ti and Pb resonances were reduced by fitting this background in the unresolved resonance region from 5 to 200 keV neutron energy with a polynomial of third order. At higher energies, the smoothing is provided by the flux correction described in the next section.

The capture yields of the Sm_2O_3 and the Au sample are plotted in Fig. 3 before and after background-subtraction. For both samples the evaluation of the background was experimentally confirmed in three different ways. (i) The Ti resonances in the critical keV region are completely eliminated in the background-subtracted spectra of both samples. (ii) The energy dependence of the capture cross section of ^{197}Au derived in the present measurement is in excellent agreement with the data reported in Ref. [23]. (iii) The background level could be experimentally verified in runs with the Sm_2O_3 sample at the energies defined by black resonance filters. Whereas the neutron beam is completely blocked in a measurement with a filter in-beam, the attenuation of the in-beam γ-ray flux has been determined by Monte Carlo simulations and was properly considered. The resulting background at energies corresponding to black resonances agrees within a few percent with the level determined with the empty Ti can, thus demonstrating that any remaining background component is negligible.

C. Absolute neutron flux determination

The total neutron flux $\Phi(E_n)$ at n_TOF has been measured with good accuracy during and after the commissioning of the facility by means of several detectors. In particular, the absolute flux was accurately determined with a calibrated fission chamber from PTB Braunschweig [8]. Consecutively, this measurement was checked by means of several detectors [9] such as SiMon, parallel-plate avalanche counters (PPAC), and fission chambers, and by the analysis of standard resonances in the capture reactions of ^{197}Au, Ag, and ^{56}Fe. An absolute normalization of the flux at low energies was also obtained by activation of a gold foil. From these measurements the

TABLE V. Flux correction factor as obtained in the simulations and from the Au measurement (see Table VI) at different neutron energies. The adopted values (third row) are obtained by renormalizing the simulated values to the experimentally determined values in the appropriate energy range.

	1–100 eV	0.1–1 keV	1–10 keV	10–100 keV	0.1–1 MeV
C_{flux}, measured values	0.180	—	—	0.186	—
C_{flux}, simulated values	0.185	0.187	0.188	0.189	0.192
C_{flux}, adopted values	0.181	0.183	0.184	0.186	0.189

energy dependence of the n_TOF total neutron fluence has been defined with an uncertainty of 2%.

However, in the present measurement only a fraction of the neutron beam is intercepted by the samples, since their diameters are always smaller than the neutron beam size. This fraction, C_{flux}, has been evaluated by normalization of the data taken with the gold sample to reproduce the standard ^{197}Au(n, γ) cross section. It was determined in two different energy regions via the respective gold cross sections and compared with the values obtained by beam profile simulations (see Table V). In the resolved resonance region between 1 and 100 eV the normalization factor was obtained by analysis of the ^{197}Au resonances with the R-matrix code SAMMY [24]. The fit was performed by keeping the parameters of the well-known resonances at 4.9, 58, and 60 eV fixed, but allowing the other resonance parameters and the normalization constant to vary. The resulting value of C_{flux} was obtained by averaging the factors extracted from the fit in different neutron energy intervals.

In the unresolved region between 5 and 200 keV, the ^{197}Au(n, γ) cross section is known with high accuracy. In this range C_{flux} can be obtained by comparing the measured (n, γ) cross section with the tabulated data [23] as indicated in Table VI. The average value of C_{flux} obtained in the energy range between 10 and 100 keV is approximately 3.3% higher than that found in the resolved resonance region. This increase is to be expected. In fact, this behavior agrees with the beam profile measurements performed at n_TOF by means of a micromegas detector [10] as well as with the results of FLUKA simulations (see Table V for details). Although the simulated values are compatible with the experimental data, a difference is still noticeable and an estimated 2% uncertainty of the method is to be assigned to the determination of C_{flux}. The experimentally determined values of C_{flux} in the energy intervals $1 < E_n < 100$ eV and $5 < E_n < 200$ keV are complemented in the remaining regions by the results of the simulations and are listed in Table V for the full energy range. The values of C_{flux} obtained from the simulations, and renormalized by 3% to match the experimental data, are adopted in the determination of the samarium capture cross section in the whole energy range. This procedure ensures the best obtainable accuracy. In fact, even if the experimental factors reported in Table VI, show large fluctuations, the averaging procedure reduces the error to the level of the estimated uncertainty.

TABLE VI. Flux correction factors experimentally determined in the unresolved resonance region, where the adopted standard neutron capture cross section of ^{197}Au [23] is available.

Energy (keV)	$\sigma_{(n,\gamma)}$ (mb)	C_{Flux}
1–1.2	—	—
1.2–1.5	—	—
1.5–1.75	—	—
1.75–2	—	—
2–2.5	—	—
2.5–3	—	—
3–4	—	—
4–5	—	—
5–7.5	1726.7	0.189
7.5–10	1215.7	0.163
10–12.5	1066.7	0.190
12.5–15	878.0	0.173
15–20	738.8	0.183
20–25	600.0	0.166
25–30	570.8	0.185
30–40	500.4	0.194
40–50	433.3	0.174
50–60	389.6	0.191
60–80	349.4	0.197
80–100	298.3	0.207
100–120	290.1	0.206
120–150	274.1	0.191
150–175	263.7	0.172
175–200	252.6	0.197
200–250	—	—
250–300	—	—
300–400	—	—
400–500	—	—
500–600	—	—
600–800	—	—
800–1000	—	—

D. Additional minor corrections

Minor corrections are related to isotopic impurities in the sample, to the self-shielding, to multiple scattering effects, and—in the resonance region—to Doppler broadening and neutron energy resolution.

In the resolved resonance region from 0.6 eV to 1 keV, these corrections are considered by the SAMMY code [24] and are automatically included in the extracted resonance parameters. The Doppler broadening is implemented according to the free-gas model with a temperature $T = 300$ K and dominates over other sources of broadening for neutron energies below 100 eV. The function describing the resolution in neutron energy [25] has been included in the fits at all energies, although this contribution is small compared to the Doppler broadening for energies below 1 keV. To account for the isotopic composition of the sample, the abundance of each isotope (Table III) was included in the SAMMY analysis together with the respective resonance parameters. Finally, the self-shielding and multiple-scattering corrections were considered according to the standard treatment in SAMMY, but these affect only the largest resonances.

TABLE VII. Correction factors for the isotopic contributions, C_{iso}, and for self-shielding and multiple scattering, C_{MS}. The ^{197}Au sample requires no isotopic correction.

Energy (keV)	Sm_2O_3		^{197}Au
	C_{iso}	C_{MS}	C_{MS}
1–1.2	0.980	0.950	0.702
1.2–1.5	0.981	0.960	0.751
1.5–1.75	0.980	0.970	0.803
1.75–2	0.980	0.980	0.823
2–2.5	0.980	0.985	0.850
2.5–3	0.979	0.990	0.893
3–4	0.981	0.995	0.930
4–5	0.978	0.997	0.951
5–7.5	0.977	1.000	0.970
7.5–10	0.978	1.005	0.998
10–12.5	0.977	1.007	1.005
12.5–15	0.977	1.008	1.015
15–20	0.978	1.010	1.021
20–25	0.977	1.010	1.025
25–30	0.974	1.009	1.028
30–40	0.973	1.009	1.029
40–50	0.971	1.010	1.027
50–60	0.962	1.010	1.028
60–80	0.969	1.009	1.029
80–100	0.972	1.009	1.028
100–120	0.955	1.009	1.028
120–150	0.958	1.008	1.025
150–175	0.955	1.009	1.025
175–200	0.957	1.008	1.024
200–250	0.958	1.008	1.022
250–300	0.958	1.008	1.020
300–400	0.944	1.007	1.019
400–500	0.937	1.007	1.018
500–600	0.928	1.008	1.016
600–800	0.918	1.006	1.015
800–1000	0.900	1.005	1.015

In the unresolved resonance region, the Doppler broadening and the neutron beam resolution can be neglected because of the averaging procedure. In this region particular care has been devoted to the self-shielding and multiple-scattering effects and to the isotopic composition of the sample (Table VII). The latter correction was determined by calculating the capture yield of the stable samarium and europium isotopes according to the JEFF-3.1 evaluated data. The JEFF-3.1 evaluation was chosen because of the good agreement with the experimental data in the unresolved region (see Sec. IV B). Only in the energy region from 5 to 200 keV, were the most recent experimental samarium capture cross sections used [26]. Averaged over the present energy bins these yields were subtracted from the measured capture yield of the Sm_2O_3 sample. The self-shielding and multiple-scattering corrections were calculated with the SESH code [27] using the statistical parameters (strength functions, average spacing, and average Γ_γ) from this work and from the most recent evaluations [28].

IV. RESULTS

A. Resolved resonance region

In the neutron-energy range between 0.65 eV and 1 keV, the capture cross section is expressed in terms of R-matrix resonance parameters obtained with the SAMMY code [24] in the Reich-Moore approximation. The background between resonances was assumed to be zero since it was subtracted in the entire energy range before the resonance analysis. In setting the neutron widths as free parameters in the R-matrix fit, a value of the scattering radius of $R' = 7.34$ fm gives the best agreement with the neutron widths obtained from the transmission measurement [6]. However, notice that our results show little sensitivity to the value of R' used in the fit, which comes into play only in the calculation of the correction for self-shielding and multiple-scattering effects. All parameters (i.e., the resonance energies as well as the partial widths) were kept free in the fit. The results obtained in this way are compared in Table VIII with the values of Ref. [6]. The quoted (1σ) uncertainties were adopted from the SAMMY analysis, and include the counting statistics and the systematic uncertainty associated with the normalization factor. Since the number of detected levels is so high (525), the complete list of the resonance parameters and additional information will be published in a separate CERN report.

The resonance shapes and the goodness of the fits indicate that the resonances below 100 eV are s waves. The ground-state spin of ^{151}Sm ($I = 5/2$) implies for s waves a total angular momentum (J) of 2 or 3, corresponding to statistical weight factors g equal to 5/12 or 7/12. Because of the poor resolution of the C_6D_6 the analysis of the γ spectra does not allow one to discriminate the spin assignment of each nuclear level. That argument is particularly true for the ^{152}Sm compound nucleus, which has a soft γ-ray spectrum and a high level density. The parameters of the smallest resonances were determined with the area analysis method using a fixed Γ_γ value. This procedure is justified since the high number of degrees of freedom in the γ cascade results in a narrow Gaussian χ^2 distribution of the Γ_γ widths with an average value of 108 ± 15 meV for the levels up to 400 eV.

As illustrated in Fig. 4, the derived resonance parameters provide a satisfactory fit of the data and moreover of the resonances of the impurity isotopes. The neutron widths (Γ_n) extracted from our fit are consistent with previous transmission data [6], but sizable differences are observed in the energy of the resonances (E_r), in the γ width (Γ_γ) (see Table VIII), and finally in the number of levels (see Figs. 4, 5, and 6). Up to 400 eV, an accurate set of resonance parameters could be derived. At higher energies the fraction of missed resonances increases and the analysis starts to be hampered by the limited resolution.

B. Unresolved resonance region

In the energy range between 1 keV and 1 MeV, the measured capture yield has been used to extract the capture cross section, according to the following relation:

$$\sigma_{sample}(E_n) = \frac{Y_{BS}(E_n) C_{iso}(E_n) C_{MS}(E_n)}{N_{Atoms} C_{flux}(E_n)}, \quad (3)$$

TABLE VIII. Resonance parameters of $n + {}^{151}$Sm compound nucleus from this work (left) compared with previous data [6] (right). All resonances are assumed to be s waves.

	n_TOF (this work)			Kirouac and Eiland [6]	
E_r (eV)	Γ_γ (meV)	$g\Gamma_n^0$ (meV)	E_r (eV)	Γ_γ (meV)	$g\Gamma_n^0$ (meV)
1.093 ± 0.001	119.48 ± 0.62	0.330 ± 0.005	1.086	98.1 ± 2	0.393 ± 0.005
1.704 ± 0.001	98.44 ± 0.34	0.139 ± 0.001	1.697	92.2 ± 4.5	0.146 ± 0.004
2.036 ± 0.002	99.89 ± 0.51	0.226 ± 0.002	2.027	81.9 ± 4.0	0.223 ± 0.005
4.132 ± 0.002	95.93 ± 0.45	0.293 ± 0.002	4.128	93.4 ± 7.7	0.263 ± 0.006
6.395 ± 0.002	107.71 ± 0.98	1.043 ± 0.027	6.392	86.7 ± 7.0	1.09 ± 0.04
10.448 ± 0.008	115.28 ± 5.25	2.122 ± 0.244	10.33	105 ± 7.0	1.91 ± 0.08
11.247 ± 0.006	109.50 ± 4.05	0.558 ± 0.062	11.13	81 ± 12	0.51 ± 0.02
12.781 ± 0.008	116.66 ± 5.15	0.219 ± 0.019	12.67	103 ± 53	0.19 ± 0.02
15.136 ± 0.007	111.16 ± 4.80	0.124 ± 0.009	15.18	96	0.108 ± 0.004
16.750 ± 0.009	98.36 ± 5.45	1.304 ± 0.117	16.80	109 ± 5	1.25 ± 0.03
17.284 ± 0.008	122.07 ± 5.10	1.913 ± 0.159	17.33	102 ± 5	1.84 ± 0.03
18.393 ± 0.009	117.53 ± 5.85	0.848 ± 0.079	18.43	117 ± 14	0.92 ± 0.11
18.564 ± 0.009	108.90 ± 5.75	0.452 ± 0.041	18.61	115 ± 24	0.47 ± 0.11
20.531 ± 0.005	124.43 ± 7.40	0.097 ± 0.007	20.65	96	0.41 ± 0.11

where Y_{BS} denotes the background-subtracted capture yield obtained via Eq. (2), N_{Atoms} is the number of atoms per barn, C_{iso} is the correction for isotopic impurities, and C_{MS} is the self-shielding and multiple-scattering corrections. The final average capture cross section of ^{151}Sm is listed in Table IX. These data are compared in Fig. 5 with the results obtained in an independent measurement at FZK [29] and with the evaluated data extracted from JEFF-3.1 [30]. The excellent agreement with the FZK measurement, which was performed with a 4π BaF$_2$ detector, confirms the reliability of the adopted experimental procedures and the respective data analyses. Up to about 200 keV the evaluated cross section from the JEFF-3.1 database follows the data rather well but underestimates the cross section at higher energies.
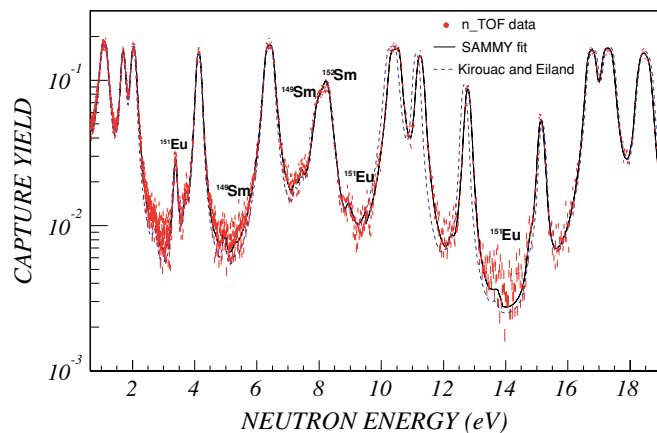

FIG. 4. (Color online) The capture yield measured with the Sm$_2$O$_3$ sample (red dots) and the SAMMY fit (black solid line) compared with the capture yield calculated with the resonance parameters of Kirouac and Eiland [6] (blue dashed line). The very small resonances are due to isotopic impurities.

TABLE IX. The ^{151}Sm(n,γ) cross section in the unresolved resonance region from 1 keV to 1 MeV.

| Energy bin	$\sigma_{(n,\gamma)}$	Uncertainty (%)		
(keV)	(b)	Stat.	Syst.	Tot.
1–1.2	24.52	0.8	4.4	4.5
1.2–1.5	23.68	0.8	4.3	4.4
1.5–1.75	21.94	1.0	4.2	4.3
1.75–2	19.76	1.2	4.2	4.3
2–2.5	15.43	1.1	4.1	4.3
2.5–3	15.36	1.3	4.1	4.3
3–4	12.78	1.2	4.1	4.3
4–5	10.04	1.4	4.1	4.3
5–7.5	8.91	2.1	2.9	3.6
7.5–10	5.85	3.0	3.1	4.3
10–12.5	5.38	3.9	2.9	4.8
12.5–15	4.26	4.9	3.2	5.8
15–20	3.82	3.8	3.2	4.9
20–25	3.52	4.6	3.5	5.8
25–30	3.13	4.5	3.1	5.5
30–40	2.69	4.4	3.2	5.5
40–50	2.17	4.8	3.4	5.9
50–60	1.90	5.2	3.3	6.2
60–80	1.66	4.1	3.6	5.5
80–100	1.30	5.1	4.6	6.9
100–120	1.09	5.4	4.9	7.2
120–150	1.00	4.8	5.4	7.2
150–175	0.69	6.7	6.2	9.2
175–200	0.78	6.4	5.9	8.7
200–250	0.68	3.3	4.4	5.5
250–300	0.50	4.1	4.4	6.0
300–400	0.42	3.1	4.5	5.5
400–500	0.37	3.6	4.6	5.9
500–600	0.28	4.0	4.6	6.1
600–800	0.25	3.2	4.7	5.7
800–1000	0.19	4.3	5.1	6.7
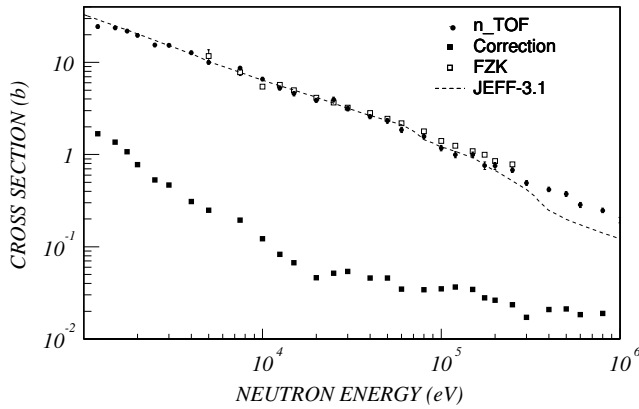
FIG. 5. The ^{151}Sm capture cross section in the unresolved resonance region compared with the recent measurement at FZK [29] (open squares) and with the JEFF-3.1 [30] evaluated data (dashed line). The corrections for isotopic impurities, self-shielding, and multiple scattering are indicated by full squares.

C. Uncertainty analysis

The statistical and systematic uncertainties given in Table IX were carefully evaluated in the various steps of data analysis and are summarized in Table X. In addition a separate error analysis has been performed, providing a detailed covariance matrix [31].

An uncertainty of less than 2% has been derived for the PHWT [16] in a complete analysis of the standard resonances of Au, Ag, and Fe. This result has been confirmed by the present analysis. A check performed with weighting functions calculated on the basis of Monte Carlo simulations with different codes has shown that—although the weighting functions differed by several percent—the effect on the final cross section ratio relative to ^{197}Au is only about 2%. Concerning the statistical uncertainty in determining the yields with the PHWT we note that the variances are not simply given by the number of events in a given neutron energy bin, but they have to be calculated by propagating these uncertainties according to the definition of the yield in Eq. (1). For the energy bins chosen in Table IX, the statistical uncertainties in the unresolved resonance region are typically 2.5%.

The uncertainty in the neutron flux determination (which includes the uncertainty in the flux shape) is associated with the fraction of the beam intercepted by the sample, indicated by the quantity C_{flux} in Sec. III C. The results obtained in different determinations of this quantity (i.e., via the low-energy resonances of Au, the standard cross sections of Au in the keV region, and FLUKA simulations), differed at most by 2.5%. It is, therefore, reasonable to adopt an overall 2% systematic uncertainty for the flux normalization.
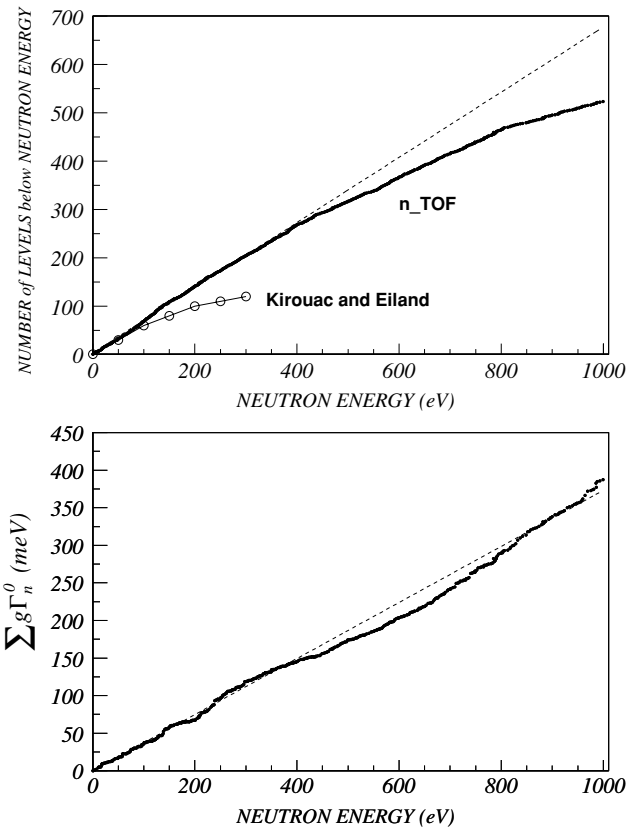

FIG. 6. The cumulative number of levels as a function of neutron energy (top) compared to the previous data [6] (open circles). The levels sequence seems to be almost complete up to 400 eV. The bottom panel shows the cumulative sum of $g\Gamma_n^0$ values for deducing the neutron strength function. In both plots the dashed lines represent a best fit to the levels up to a neutron energy of 400 eV.

The number of atoms in the samarium sample has been derived by mass spectrometry at ORNL immediately after the separation. The composition at the time of the measurement is consistent with the results of the largest ^{151}Sm resonances at low energy and with the detected ^{151}Eu resonances (Fig. 4). The resonance fits and the spectrometric analysis indicate an uncertainty of 0.1% for the isotopic abundances, derived essentially from the uncertainty of the ^{151}Sm half-life. In the unresolved resonance region (Table VII) the isotopic correction of the samarium sample is quite important, especially at higher energy. This correction factor is calculated mainly according to the evaluated capture cross sections of the stable samarium and europium isotopes from the JEFF-3.1 database. Wherever possible, this information was complemented by recent experimental data [26]. The cross

TABLE X. Contributions to the uncertainty of the ^{151}Sm(n, γ) cross section (in percent).

Sample	WF	Flux	Sample composition	Self-shielding and multiple scattering	Systematic uncertainty	Statistical uncertainty	Total uncertainty
Sm$_2$O$_3$	2	2	0.5–2.5	0.1–1	3–6.2	0.8–6.4	3.5–9
Au	2	—	—	0.1	2	0.5–3.5	2–4

sections in the different data libraries show variations of 30% on average, which propagate into the capture cross sections, introducing energy-dependent uncertainties between 0.5% and 2.5%.

The self-shielding and multiple-scattering corrections were calculated with the SESH code using the total, elastic, and capture cross sections of Sm and Au. In this case, the main uncertainties originate from the nuclear parameters used for the SESH calculations. However, these corrections are comparably small and contribute to uncertainty by less than 1% in the whole energy region.

In conclusion, the overall uncertainty of the ^{151}Sm capture cross sections in the unresolved resonance region is 6% on average. In addition to the counting statistics, this uncertainty is essentially determined by the PHWT and the flux determination (Table X). Significant contributions from minor uncertainties (i.e., owing to isotopic corrections, self-shielding, and multiple scattering) are mostly limited to neutron energies above 100 keV (Fig. 5).

V. IMPLICATIONS

A. Nuclear structure

Nuclear structure effects at excitation energies around the neutron separation energy can be investigated by neutron resonance studies. In this respect the most relevant quantities are the density of nuclear compound states, their statistical distribution, and the distribution of their widths. The statistical analysis of the high-resolution data obtained in this work yields the cumulative number of s-wave compound states at the neutron separation energy of 8.258 MeV (top panel of Fig. 6). The analysis includes both possible values of the total angular momentum that are $J = 2$ and $J = 3$ for the s-wave resonances. The level sequence is satisfactorily resolved in the energy range up to 400 eV, whereas an increasing number of levels is evidently missed at higher energies. To extract the average level spacing of the s-wave levels $\langle D_0 \rangle$, we have performed a maximum-likelihood fit using a Wigner distribution. This approach yields a value of $\langle D_0 \rangle = 1.49 \pm 0.07$ eV, equivalent to a nuclear level density of $(6.71 \pm 0.31) \times 10^5$ MeV^{-1} at 8.258 MeV. This result is also confirmed by the fitting of the cumulative number of levels with a third degree polynomial, as illustrated in Fig. 6. However, contrarily to our expectation, the distribution of the spacing follows nicely the shape of a single-level Wigner distribution. In fact according to a two-levels Wigner distribution (for the two different J values), the spacing distribution should be more broadened and more concentrated at low values ($D_0 \leqslant 0.3$ eV) whereas in our sample of levels this region is scarcely populated. Nevertheless, from this analysis, we can conclude that the contamination of p-wave levels in our set of resonances is very improbable.

To estimate the number of missing levels, we have compared the reduced neutron width $g\Gamma_n^0$ of our set of resonances (up to 400 eV) with a Porter-Thomas (PT) distribution for a single-level population $\chi_{v=1}^2$. In fact, the integration of the $\chi_{v=1}^2$ function provides the total number of expected levels
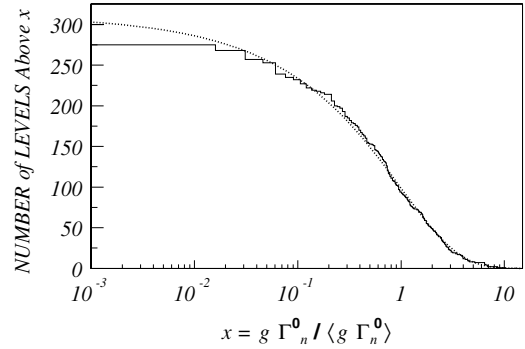

FIG. 7. Histogram representing the cumulated number of levels having value larger than x. The dotted line indicates the fit of the histogram by means of Eq. (4) (see text for details). The levels start to disappear at very low values of x. In this analysis, only the levels up to 400 eV neutron energy are considered.

according to the relation

$$N(x) = N_0[1 - \mathrm{erf}(\sqrt{x/2})], \qquad (4)$$

with $x = g\Gamma_n^0/\langle \Gamma_n^0 \rangle$ and N_0 the total number of expected s-wave levels. The result of the fit, leaving N_0 free to vary, is illustrated in Fig. 7 and indicates that we are missing ∼10% of levels ($N_0 = 305 \pm 6$) at very low $g\Gamma_n^0$. In this case, it is important to remark that the PT function correctively describes the $g\Gamma_n^0$ distribution if there are no correlations between different levels and is valid for a single-level population.

The most stringent test of the completeness of the level sequence is the Dyson-Mehta (DM) Δ_3 statistics [32], which yields predictions in good agreement with experimental data, especially for samarium and other rare-earth elements [6]. For the two populations corresponding to the two J values, the theoretical DM Δ_3 value is 0.99 ± 0.22, smaller than the Δ_3 value of 3.0 ± 0.4 obtained from the experimental data. This difference may well be due to the loss of a few levels in the long sequence of ^{151}Sm resonances, indicating that we are missing some weak s-wave resonances.

To have a further theoretical check of our assumption that all the observed resonances up to 400 eV are s-wave resonances, and that they constitute most of the nuclear levels in this region, we have calculated both the s-wave resonance spacing D_0 and the p-wave resonance spacing D_1 in a micro-canonical model of nuclear level densities, where the intrinsic contribution, computed by Monte Carlo sampling of noncollective nuclear excitations, is folded with a collective contribution generated by the interacting boson model [33]. Our theoretical results are as follows: $\langle D_0 \rangle = 1.20 \pm 0.06$ eV and $\langle D_1 \rangle = 0.59 \pm 0.03$ eV. The former is slightly lower than our experimental value but consistent with the assumption that the large majority of the observed resonances are of s-wave type. The latter indicates that there are twice as many unobserved p-wave resonances as s-wave resonances in this energy range. The theoretical value of the $\langle D_0 \rangle/\langle D_1 \rangle$ ratio is consistent with the experimental results for nuclei in the $A = 130$ mass region, such as Ba isotopes, where p-wave resonances are observed [34].

Another fundamental quantity related to nuclear properties is the neutron strength function. The bottom panel of Fig. 6 shows the fit of the cumulative sum of the reduced neutron widths as a function of the complete level sequence up to 400 eV for deriving the *s*-wave neutron strength function, which is rather insensitive to missing levels but depends almost exclusively on the neutron widths. The cumulative sum of reduced neutron widths continues to rise linearly toward higher energies, in spite of the missing levels beyond 400 eV. The fit with a straight line furnishes a strength function of $\langle S_0 \rangle = (3.87 \pm 0.33) \times 10^{-4}$, in agreement with but more accurate than the previous value [6] of $(3.65 \pm 0.48) \times 10^{-4}$.

The average level spacing represents a reliable measure of the nuclear level density close to the neutron separation energy. To study the nuclear level densities in the six samarium isotopes, the Fermi-gas level density parameter a was calculated with the Gilbert and Cameron formula (Eq. (4) in Ref. [35]) using the pairing energies δ, the spin cutoff parameters σ according to the Cameron and Elkin semi-empirical mass formula [36], and the most recent values of the average level spacing (Table XI). As illustrated in Fig. 8, the result confirms the conclusions of Kirouac and Eiland for the samarium isotopes [6] and of Karzhavina *et al.* [37] for the neodymium isotopes that the level density decreases near shell closure ($N = 82$, $A = 148$), whereas it approaches a maximum when the shell is half-filled ($84 < N < 90$) owing to the increase of particles and holes in the shell [38].

The shell-corrected level density parameter was obtained from the expression

$$a = \tilde{a} \left[1 + \frac{E_{\text{sh}}}{U} (1 - e^{-\gamma U}) \right], \qquad (5)$$

where the shell-correction energy E_{sh} and the damping parameter γ are calculated according to the liquid drop model and nuclear systematics [35]. The excitation energy is defined as $U = S_n - \delta$. Except for the compound nucleus ^{155}Sm, the corrected parameters $\tilde{a}$ exhibit the expected linear dependence on mass number (Fig. 8). The 10% uncertainty indicated for the a and $\tilde{a}$ parameters in Fig. 8 corresponds
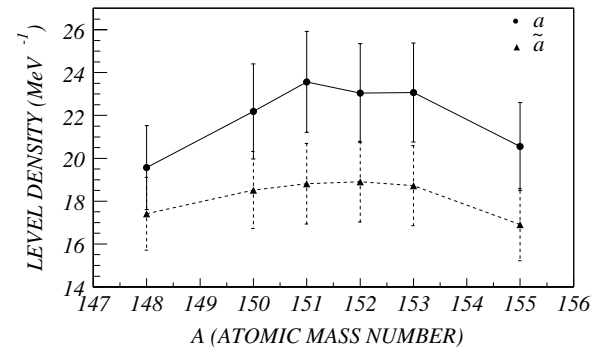

FIG. 8. Level density parameters of the samarium isotopes with and without corrections for shell effects vs the mass of the compound nucleus. The curves are intended to guide the eye.

to the level of agreement with recent systematic studies [39,40]. Within the limits of the approximations used in the theoretical models (Fermi gas and liquid drop) and the related parameters (spin cutoff and pairing energies) such analyses can provide information on the level density of isotopes, where no experimental data are available (e.g., for ^{153}Sm).

The level density parameters of ^{155}Sm and to a lesser extent of ^{153}Sm deviate significantly from linearity. Since the average level spacing of both nuclei was, in fact, obtained by transmission measurements at the same facility [41], this discrepancy may not originate from the experimental information but may indicate the possible closure of a subshell that the liquid drop model does not correctly take into account.

B. Nuclear reactors

The samarium isotopes are relevant neutron poisons in conventional reactors because of the huge thermal cross sections of ^{149}Sm and ^{151}Sm and in fast reactor systems because ^{151}Sm has one of the largest capture cross sections in the intermediate energy region between 1 keV and 1 MeV. Accordingly, accurate experimental data have been requested in particular for the keV region [2,42,43]. The main quantities formulated in these requests are the neutron capture cross sections at thermal energy, σ_{th}, and the resonance integral

$$RI = \int_{0.5\,\text{eV}}^{1\,\text{MeV}} \sigma_{\gamma}(E_n)/E_n \, dE_n. \qquad (6)$$

Though the total and capture cross section at thermal energy, σ_{th}, cannot be directly deduced from the present n_TOF data because the accessible neutron energy range starts at 0.6 eV, it can be obtained by adding the bound-state contribution from the transmission measurement and the contribution from the resonance region. Kirouac and Eiland [6] have determined a thermal total cross section of 15,200 b with a strong non-1/v trend and a 2% contribution from the resonance region. With the improved resonance parameters of this work, the resonance component is slightly higher, leading to a

TABLE XI. Level density of the samarium compound nuclei with and without shell corrections. The main quantities used in the calculations are indicated.

Compound nucleus	Spin cutoff σ [36]	Pairing energy δ (MeV) [35]	Average spacing $\langle D_0 \rangle$ (eV)	Fermi level density a (MeV^{-1})	Corrected Fermi level density $\tilde{a}$ (MeV^{-1})
^{148}Sm	5.17	2.14	6.05 [28]	19.57	17.41
^{150}Sm	5.33	2.21	2.45 [28]	22.19	18.52
^{151}Sm	5.04	1.22	46.5 [28]	23.57	18.81
^{152}Sm	5.42	2.32	1.48 [this work]	23.05	18.91
^{153}Sm	5.10	1.22	34.6 [41]	23.07	18.72
^{155}Sm	5.00	1.22	115.0 [41]	20.55	16.91

TABLE XII. Thermal cross sections and resonance integral of ^{149}Sm(n, γ), ^{150}Sm(n, γ), and ^{151}Sm(n, γ) reactions.

	^{149}Sm [45]	^{150}Sm [45]	^{151}Sm [6]	^{151}Sm [this work]
$\sigma_{\text{tott-thermal}}$ (b)	—	—	15200	$15250^a \pm 534$
$\sigma_{\gamma\text{-thermal}}$ (b)	39920	103	—	$15020^a \pm 525$
RI (b)	3367	307	3520 ± 160	$3575^a \pm 120$

^{a}Values estimated via bound state (see text and Ref. [6]).

thermal capture cross section of 15,020 b. By using the same approach and taking in account the transmission data and noting that there is one more level at 0.456 eV not estimated in this work but measured previously [6], the resonance integral has been estimated as 3575 ± 210 b, in perfect agreement with the previous determination of 3520 ± 160 b. Notice that almost 70% of the resonance integral is due to the energy region from 0.5 to 30 eV. The results are summarized in Table XII and show that the measured and evaluated capture cross sections of ^{149}Sm [44] and ^{151}Sm in the thermal and in the resolved region agree within a few percent. However, considerable differences remain in the unresolved region for several isotopes of interest for the design of innovative reactors [45].

In particular, the necessary safety margin for the sub-criticality of an ADS, the analysis of the reactor dynamical behavior, and the validation of computational methods [46] require accurate capture cross sections from 1 keV up to 1 MeV neutron energy, mainly for the fuel isotopes but also for the fission fragments and for structural materials [47]. The impact of the fission products was investigated by a sensitivity analysis, where we calculated the variation of the reactivity in the core of the Energy Amplifier Demonstration Facility [45] (EADF) by using the EA-MC Monte Carlo code [48] and three nuclear data libraries, ENDF/B-VI.8 [49], JENDL-3.3 [50], and JEFF-3.1 [30], the latter of which was chosen as the reference library. The largest differences in the neutron data were found between the fission and the capture cross sections of the fuel isotopes ^{238}U, ^{240}Pu, ^{241}Pu, and ^{232}Th, which affect the uncertainty of the source multiplication factor k_{src} by 2000 pcm; those inaccuracies in the ADS calculations are much larger than the precision required which ranges between 10 pcm [43] and 100 pcm [51]. The higher accuracy of the nuclear data in EADF with respect to the thermal reactors is essentially motivated by three reasons. First, the EADF is a subcritical reactor and operates with a very fast neutron spectrum, which implies a shorter time-scale for reactor control [46]. Second, the fuel is composed by several kinds of isotopes (fissiles, fertiles, and minor actinides) with relative decay chains. In some cases, the inaccuracies on the nuclear data of the different isotopes are compensating in the Monte Carlo calculations, but sometimes they are not. Finally, unlike in thermal reactors where the neutron multiplication factor decreases as a function of burnup, in an ADS k_{src} (right axis in Fig. 9) rises, propagating this increase to the reactivity changes (see $\Delta k_\infty/k_\infty$ in Fig. 9). Therefore in an ADS, the differences induced by uncertainties on the nuclear data can be minimized simply by providing accurate cross sections to the simulation code.
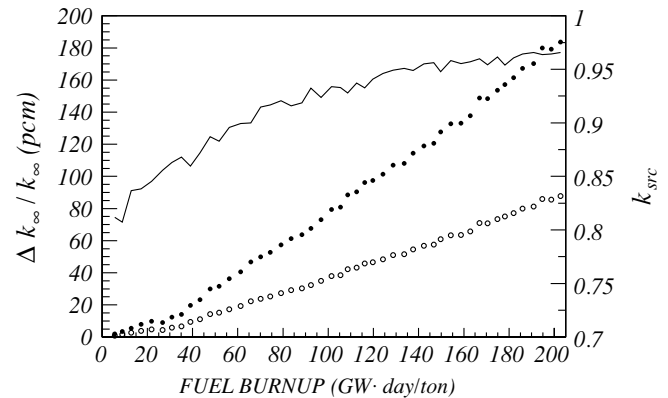

FIG. 9. Variation of k_∞ as a function of burnup (1 pcm $= 10^{-5}$) calculated for an EADF [45] by using the JENDL-3.3 [50] and JEFF-3.1 [30] nuclear data libraries (full circles). Significantly smaller variations are achieved by using experimental data for five important isotopes (empty circles; see the text for details). The black line indicates the evolution of the neutron multiplication k_{src} (right axis) for the same system.

Instead of using a source multiplication factor k_{src}, which has to account for all contributions affecting the neutron balance in an ADS, such as the geometry, the spatial distribution of the flux, the coolant, the structural materials, and in particular the external neutron source [52], the present study was restricted to the simpler case of k_∞, the infinite multiplication factor corresponding to a reactor of infinite dimensions. By assuming a (U-Pu)O$_2$ fueled reactor with 80%^{238}U, 12%^{239}Pu, 6%^{240}Pu, and 2%^{241}Pu, the sensitivity of k_∞ to specific fission product cross sections has been investigated.

The changes $\Delta k_\infty/k_\infty$ are calculated by keeping the cross sections of the fuel isotopes from the reference library fixed but adopting the capture cross sections of the fission products from different databases. The largest differences were found to result from the JEFF and JENDL libraries, as shown in Fig. 9. Since these differences increase with burnup, the related uncertainties, especially for a typical burnup of 150 GW day/ton, are larger than the required accuracy. We then replaced the capture cross sections of five important fission products by recent experimental data (i.e., for ^{151}Sm [this work], ^{149}Sm [26], ^{145}Nd [53], ^{147}Pm [54], and ^{135}Cs [55]). These nuclei are all abundantly produced in nuclear reactors, have high capture cross sections, and show the largest variations between the nuclear data libraries, as illustrated in Fig. 10 where examples of the one-group [42] capture cross sections $\langle\sigma_{n,\gamma}\rangle$ weighted by the relative fission yield are shown.

Note that the variations Δk_∞ correspond only to the differences between evaluated data but neglect the intrinsic cross section uncertainties and that the experimental cross sections do not cover the whole neutron energy range from 1 keV to 1 MeV. For this reason the evaluations that agree best with the experimental data are used in the remaining parts of the spectrum. The net result of these choices is a considerable reduction of Δk_∞, thus emphasizing the importance of reliable cross sections.

In addition to the isotopic composition, Δk_∞ depends strongly on the neutron energy distribution. The calculations
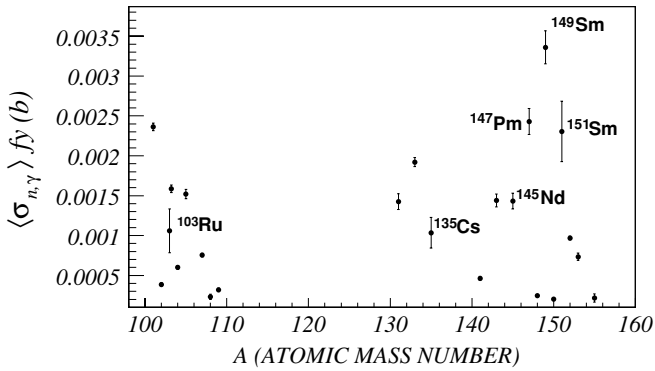
FIG. 10. The product of one-group capture cross sections $\langle\sigma_{n,\gamma}\rangle$ and fission yields fy, as a function of the atomic mass number for an EADF [45] device. The one-group cross sections are calculated using the neutron flux of the EADF and the capture cross sections of JEFF-3.1 [30]. The uncertainties are estimated by comparison with other data libraries.

of $\Delta k_{\infty}/k_{\infty}$ are performed with the typical energy amplifier spectrum peaked between 0.1 and 1 MeV. The variations of Δk_{∞} are larger by up to an order of magnitude with respect to the standard case when the neutron spectrum becomes softer and vice versa. This behavior of Δk_{∞} is correlated with the fact that the capture cross sections of the fission product nuclei decrease with neutron energy, whereas the fission cross sections of the fissile isotopes remain almost constant.

In spite of this strong sensitivity to the neutron cross sections at higher burnup, the EADF is a safe reactor. In fact, the source multiplication factor is always well below the critical value (see Fig. 9) and the variations of $\Delta k_{\mathrm{src}}/k_{\mathrm{src}}$, calculated by propagating the relative contributions of $\Delta k_{\infty}/k_{\infty}$, do not basically alter this state.

As far as the possible incineration of the ^{151}Sm and other fission products is concerned, the transmutation option with an ADS appears to be questionable in several cases. Unlike the minor actinides, the fission products represent a strong neutron sink throughout the incineration process. Therefore, the fuel cannot be heavily loaded with such isotopes. In these cases the priority is to reduce the radiotoxicity of the long-lived fission products with half-lives longer than 10^5 yr (e.g., ^{93}Zr, ^{99}Tc, and ^{135}Cs [56]). For the short-lived fission products (^{151}Sm, ^{137}Cs, and ^{90}Sr) the proposed solution is an interim storage facility.

In conclusion, knowledge of the capture cross sections of comparably few relevant fission product isotopes (i.e., Zr, Ru, Xe, Cs, Nd, Pm, Sm, and Eu; see Fig. 10) in a wide energy range (1 keV–1 MeV) and with uncertainties below 5% may suffice to improve, on the nuclear data side, the accuracy of ADS Monte Carlo calculations up to the required limit ($\leqslant 100$ pcm). For a complete sensitivity analysis of the neutron balance it will be necessary to consider the cross section uncertainties of the fuel and of the structural materials and to perform a correlated analysis including all uncertainties of the reactor operations (imperfection in the geometry, in the temperature dependence, and in the power and flow variations). In this context, the experimental capture cross section of the fission product ^{151}Sm represents an important initial milestone.

C. Nuclear astrophysics

The analysis of *s*-process branchings provides important constraints for models of helium-shell burning in low-mass asymptotic giant branch (AGB) stars [1]. The particular branch point ^{151}Sm represents a case where the β-decay rate exhibits a pronounced temperature dependence; the corresponding reduction of the half-life from the terrestrial value of 93 yr to a few years in the stellar environment [57] initiates a number of branchings in the reaction network of the Sm-Eu-Gd region (Fig. 1). The two main branchings at ^{151}Sm and ^{154}Eu affect the production of the *s*-only isotopes ^{152}Gd and ^{154}Gd, which are shielded against the *r* process by their stable isobars. All other nuclei involved in the branchings are mainly produced by the *r* process.

By neglecting minor corrections the branching factor at ^{151}Sm can be written as

$$f_{\beta} = \frac{(\langle\sigma\rangle N)_{^{152}\mathrm{Gd}}}{(\langle\sigma\rangle N)_{^{150}\mathrm{Sm}}} = \frac{\lambda_{^{151}\mathrm{Sm}}}{\lambda_{^{151}\mathrm{Sm}} + n_n \langle\sigma v\rangle_{^{151}\mathrm{Sm}}}, \qquad (7)$$

where $\langle\sigma\rangle$ is the Maxwellian-averaged capture cross section (MACS), N is the *s*-process abundance, n_n is the neutron density, v is the neutron relative velocity, and $\lambda_{^{151}\mathrm{Sm}}$ is the stellar β-decay rate of ^{151}Sm. The *p*-process contribution to ^{152}Gd is not yet considered in Eq. (7). The MACS of all stable isotopes of this branching have been determined with accuracies of $\leqslant 2\%$, but for ^{151}Sm only comparably uncertain statistical model calculations were available so far. As for branching at ^{152}Eu (suffering β^-, β^+, and electron capture), the β-decay rate is enhanced by five orders of magnitude at $T = 3 \times 10^8$ K [57], so that almost all the neutron fluence deriving from ^{151}Eu directly feeds ^{152}Gd. The other branching at ^{153}Sm is marginally effective, because of its very fast β-decay rate. During the neutron exposure in the thermal pulse, the average half-life of ^{151}Sm is decreased by an order of magnitude from its experimental terrestrial value of 93 yr to 7.6 yr [57].

The MACS are calculated using the n_TOF capture cross section from 0.1 to 500 keV for a complete set of thermal energies between 5 and 100 keV. The contribution of the resolved resonance region was obtained by using the resonance parameters; the unresolved part is calculated by folding the capture cross section with the Maxwellian distribution numerically (Table XIII). As reported in our previous paper [58], the MACS at 30 keV was determined to be 3.08 ± 0.15 b. This result is confirmed by the recent measurement at FKZ [29] and is considerably higher than previous theoretical predictions, which varied between 1.5 and 2.8 b.

In the classical *s*-process approach, where the neutron density and the temperature are assumed to be constant in time, Eq. (7) can be solved directly for the stellar decay rate of ^{151}Sm, which in turns yields the effective *s*-process temperature (the neutron density being determined by other branchings not sensitive to the temperature). The most recent classical analyses [59] have demonstrated that consistent solutions for a unique *s*-process temperature and neutron density do not exist. Instead, stellar models of low-mass thermally pulsing AGB stars provide more realistic alternatives to the classical scenario [60]. According to this model, more

MEASUREMENT OF THE ^{151}Sm(n, γ) CROSS SECTION FROM . . .

PHYSICAL REVIEW C **73**, 034604 (2006)

TABLE XIII. Maxwellian-averaged (n, γ) cross section of ^{151}Sm[a].

Thermal energy (keV)	$\langle\sigma\rangle_{\text{RRR}}$ (b)	$\langle\sigma\rangle_{\text{URR}}$ (b)	$\langle\sigma\rangle_{\text{tot}}$ (b)
5	1.16	9.49	10.65 ± 0.50
7.5	0.54	7.42	7.96 ± 0.39
10	0.31	6.19	6.50 ± 0.32
12.5	0.20	5.37	5.57 ± 0.27
15	0.14	4.78	4.92 ± 0.24
17.5	0.10	4.34	4.44 ± 0.21
20	0.08	3.98	4.06 ± 0.19
25	0.05	3.44	3.49 ± 0.16
30	0.03	3.05	3.08 ± 0.15
35	0.03	2.75	2.78 ± 0.14
40	0.02	2.51	2.53 ± 0.12
45	0.02	2.31	2.33 ± 0.11
50	0.01	2.14	2.15 ± 0.10
60	0.01	1.88	1.89 ± 0.09
70	0.006	1.68	1.69 ± 0.08
85	0.005	1.45	1.46 ± 0.07
100	0.003	1.29	1.29 ± 0.06

[a]Contributions in the resolved and unresolved resonance region are listed separately.

than 90% of the neutron exposure is due to the ^{13}C$(\alpha, n)^{16}$O reaction, which operates at temperatures around 100 MK ($kT \approx 8$ keV) in a tiny layer at the top of the He intershell (the so-called ^{13}C pocket [61]). Neutrons are released in radiative conditions in the interpulse phase, with a high neutron exposure and a low neutron density of 10^7 cm^{-3} over a relatively long period of some 10^4 yr. This phase is followed by He-shell-burning episodes that are characterized by higher temperatures ($kT = 20$–25 keV) and shorter times (5–10 yr). At these temperatures, the ^{22}Ne$(\alpha, n)^{25}$Mg neutron source is marginally activated and gives rise to a neutron burst of a small neutron exposure but with a high peak neutron density of about 10^{11} cm^{-3} (Fig. 11). During these thermal pulses, the whole He intershell (a thin region between the H shell and the He shell) becomes convective. (For details see the review by Busso, Gallino, and Wasserburg [61].)

The simultaneous enhancement of neutron density and temperature is reflected in the evolution of the isotopic abundances during the 15th thermal pulse shown in Fig. 11 for a star of 1.5 solar masses and half the solar metallicity. The upper part of Fig. 11 describes the abundance evolution in the neutron capture part of the ^{151}Sm branching, whereas the lower part illustrates the corresponding abundances in the β-decay part. At the beginning of the pulse, the ^{151}Sm abundance grows and remains almost constant until the end of the pulse because the decrease in neutron density is just compensated by the effect of temperature on the half-life of ^{151}Sm. Since only a small fraction of ^{151}Sm undergoes β decay during the neutron exposure, the ^{152}Sm abundance is not noticeably affected and remains practically constant. Only isotopes related to the minor branches feel the strong variation of neutron density and temperature in the flash, in particular ^{154}Sm in the upper and ^{151}Eu and ^{152}Gd and ^{154}Gd in the lower panel of Fig. 11. Note, however, that the abundance of these three isotopes is restored at the end of the thermal pulse by the effect of the final
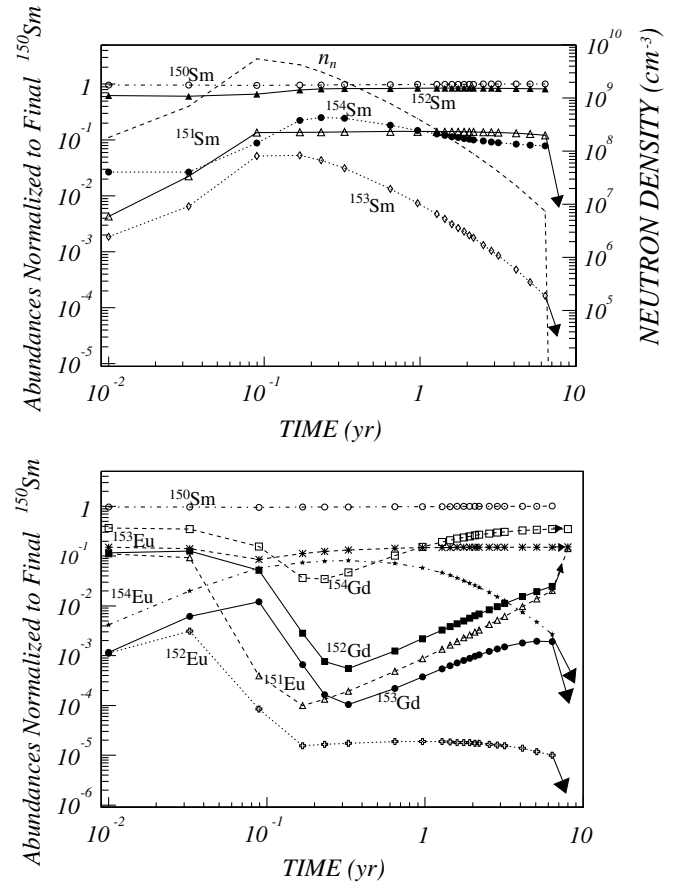

FIG. 11. The abundance evolution of isotopes in the Sm-Eu-Gd region and of the average neutron density (right axis) in the He intershell during the 15th convective thermal pulse calculated for a star of 1.5 solar masses with half the solar metallicity [60]. All values are normalized to the final ^{150}Sm abundance. Arrows indicate the decay of radioactive isotopes and the in-growth of their daughter nuclei in the interpulse phase.

decrease of the average neutron density, taking account of the high MACS of all nuclides involved in this region. The neutron exposure by the ^{22}Ne source increases with pulse number, owing to the slight increase of the maximum temperature at the bottom of each convective thermal pulse. Consequently, the s-process material cumulatively mixed with the envelope by recurrent third dredge-up episodes [61] keeps memory of all the neutron exposures induced in the ^{13}C pockets and in the thermal pulses. This s-process material is then remixed with the interstellar medium by the strong stellar winds during the whole AGB phase.

At the end of the thermal pulse, the remaining unstable isotopes decay and contribute to the final abundances of ^{151}Eu, ^{153}Eu, and ^{154}Gd. The ^{152}Gd abundance is not affected in this last phase because the ^{152}Eu abundance is already negligible at this point. The most important radiogenic decay, by ^{151}Sm, after the occurrence of the neutron burst involves an increase of the final abundance of ^{151}Eu by a factor of 7. This means in particular that the production factor of ^{151}Eu is insensitive to its MACS. All freshly synthesized s-process

TABLE XIV. Sensitivity of *s*-process production factors[a] with respect to remaining nuclear physics uncertainties (all values relative to the *s*-only isotope ^{150}Sm). The largest variations are reported in bold face.

Isotope	Standard	$\lambda_\beta(^{151}\text{Sm}) \times 1.5$	$\langle\sigma\rangle\,(^{151}\text{Sm}) \times 0.9$	$\langle\sigma\rangle\,(^{153}\text{Eu}) \times 1.1$	$\lambda_\beta(^{153}\text{Sm}) \times 1.5$	$\langle\sigma\rangle\,(^{154}\text{Eu}) \times 0.7$	$\lambda_\beta(^{154}\text{Eu}) \times 1.5$
^{150}Sm	1	1	1	1	1	1	1
^{152}Sm	0.226	0.222	0.225	0.226	0.226	0.226	0.226
^{154}Sm	0.025	0.025	0.025	0.025	**0.018**	0.025	0.025
^{151}Eu	0.058	0.057	**0.063**	0.058	0.058	0.058	0.058
^{153}Eu	0.057	0.057	0.057	0.052	0.057	0.057	0.057
^{152}Gd	0.781	**1.105**	**0.852**	0.781	0.781	0.781	0.781
^{154}Gd	0.909	0.911	0.909	0.910	0.910	**0.957**	**0.944**

[a]For the average 1.5 and 3 solar mass AGB models of half the solar metallicity. (See Ref. [64] for discussion.)

products are cumulatively mixed by third dredge-up episodes into the envelope of the star and later ejected into the interstellar medium by stellar winds.

Using the present MACS of ^{151}Sm and the most recent values for the stable isotopes together with additional information concerning the stellar enhancement factors [62] and β-decay rates [57], the investigated stellar model predicts an *s*-process production of 78% for ^{152}Gd and 91% for ^{154}Gd with respect to the solar abundances [63]. All other isotopes exhibit a dominant *r*-process origin with only small *s* contributions of 6% for ^{151}Eu and ^{153}Eu, 23% for ^{152}Sm, and 2.5% for ^{154}Sm (Table XIV). Compared to a previous analysis [64] we obtain a 10% higher and a 4% lower abundance for ^{152}Gd and ^{154}Gd, respectively. The missing fraction of the ^{152}Gd abundance can in principle be accounted for by a 22% contribution from the *p* process, consistent with the abundances of the closest *p*-only isotopes ^{144}Sm, ^{156}Dy, and ^{158}Dy. (For a discussion see the contribution of Wisshak *et al.* [29]). It is important to note that the theoretical stellar models of the *p* process predict a $\sim$12% contribution to the solar ^{152}Gd abundance [65,66].

The europium abundances obtained in the present analysis are of considerable interest for recent observations in metal-poor stars showing a distinct *s*-process enhancement. Whereas the ^{151}Eu fraction $fr(^{151}\text{Eu}) = {}^{151}\text{Eu}/({}^{151}\text{Eu} + {}^{153}\text{Eu}) = 0.49$ [61] obtained with stellar *s*-process models is rather similar to the solar value of 0.478 [63], the newest hyperfine splitting analyses of such stars indicate significantly larger values between 0.54 and 0.66 [67]. It should, however, be noted that the observational data exhibit non-negligible uncertainties because they are derived from only three europium lines and depend also on the stellar atmospheric parameters. For metal-poor stars with strong *r*-process enhancement the corresponding analysis yields a fraction of $\sim$0.5 [68]. Moreover, *s*-enhanced stars also show a large scatter in the abundance ratio of europium and iron compared to stars of similar metallicity [69].

To investigate possible solutions within the present AGB models, the stellar enhancement factor of the ^{151}Sm cross section and the β-decay rate were changed within plausible limits. These variations are motivated by the existence of low-lying excited states in the europium and in the odd samarium isotopes, which are significantly populated at *s*-process temperatures. At present, these quantities are only theoretically known, and their large uncertainties [56,70] represent the remaining nuclear ambiguities for *s*-process

studies in the mass region around $A = 150$. The results of this sensitivity analysis are summarized in Table XIV, where the standard case is listed in the second column. Variation of the β-decay rate and the MACS of ^{151}Sm by 50% and 10%, respectively, gives obviously rise to a significant enhancement of the ^{152}Gd abundance or even to an overproduction of this isotope. In contrast, variations of the β-decay rate and or the MACS of ^{153}Sm affect only the small *s*-process contribution of ^{154}Sm but do not contribute to the europium or gadolinium production. Similar changes of the parameters for ^{152}Eu have no global effects on the final isotopic abundances. Concerning ^{153}Eu, the only effect of a 10% increase of its MACS is the corresponding 10% decrease of its *s*-process abundance. In this case the stellar model yields a ^{151}Eu fraction of $fr(^{151}\text{Eu}) = 0.54$, marginally compatible with the observations in metal-poor stars. A further increase of this value could only be achieved if the stellar enhancement factor of ^{151}Eu were smaller than current expectations [59]. The last two columns of Table XIV deal with the *s* abundance of ^{154}Gd, which is not fully accounted for. This deficiency cannot be compensated by the *p* process, which contributes only $\leqslant$2% to the abundance of ^{154}Gd. Since the cross section of the unstable branch point ^{154}Eu is obtained from statistical model calculations the 30% variation is certainly justified and almost sufficient to fully reproduce the missing ^{154}Gd abundance (Table XIV, column 7). Whether this explanation holds or whether the solution implies a large variation of the β-decay rate (Table XIV, column 8) needs to be decided by an experimental determination of the ^{154}Eu cross section. The MACS of ^{152}Gd and ^{154}Gd have been determined experimentally with accuracies of 1.6% and 1.2%, respectively [71]. The relative solar abundances of all lanthanides, including Sm, Eu, and Gd, are also well defined [63].

VI. CONCLUSIONS

The (n, γ) cross section of the unstable isotope ^{151}Sm has been measured over a wide range of neutron energies using the n_TOF facility at CERN. The reliability of the measurement and the accuracy of the results have been demonstrated by a complete presentation of the data analysis and a detailed discussion of the related uncertainties. In the resolved resonance region the obtained physical quantities (i.e., resonance parameters, resonance integral, level

densities, neutron strength function, and average γ widths) were found consistent with but significantly more accurate than previous results obtained in a transmission measurement [6]. This agreement is restricted to lower energies, whereas the present results benefit greatly from the excellent energy resolution of the n_TOF facility, which allowed us to detect most of the resonance structure up to 400 eV, resulting in five times more resonances being resolved than in the transmission measurement. In the unresolved region, where the measurement could be extended up to 1 MeV, excellent agreement was obtained with the experiment of Wisshak *et al.* [29], which was performed with a 4π BaF$_2$ detector.

The implications of the present results were discussed with respect to neutron physics, nuclear astrophysics, and nuclear technology.

[1] F. Käppeler, Prog. Nucl. Part. Phys. **43**, 419 (1999).

[2] *NEA High Priority Nuclear Data Request List*, OECD-NEA, Nuclear Science Committee, 1998.

[3] K. Fujimura, T. Sanda, S. Moro, M. Saito, and H. Sekimoto, Prog. Nucl. Energy **40**, 587 (2002).

[4] C. Rubbia *et al.*, CERN/AT/95-53, 1995.

[5] N. J. Pattenden, Nucl. Sci. Eng. **17**, 371 (1963).

[6] G. J. Kirouac and H. M. Eiland, Phys. Rev. C **11**, 895 (1975).

[7] n_TOF Collaboration, Report CERN-SPSC 99-8, CERN, 1999.

[8] C. Borcea *et al.*, Nucl. Instrum. Methods A **513**, 524 (2003).

[9] n_TOF Collaboration, Report CERN-INTC-O-011, CERN, 2003.

[10] J. Pancin *et al.*, Nucl. Instrum. Methods A **524**, 102 (2004).

[11] S. Marrone *et al.*, Nucl. Instrum. Methods A **517**, 389 (2004).

[12] R. Plag, M. Heil, F. Käppeler, P. Pavlopoulos, R. Reifarth, and K. Wisshak, Nucl. Instrum. Methods A **496**, 425 (2003).

[13] U. Abbondanno *et al.*, Nucl. Instrum. Methods A **538**, 692 (2005).

[14] R. L. Macklin and J. H. Gibbons, Phys. Rev. **159**, 1007 (1967).

[15] P. E. Koehler, R. R. Spencer, R. R. Winters, K. H. Guber, J. A. Harvey, N. W. Hill, and M. S. Smith, Phys. Rev. C **54**, 1463 (1996).

[16] U. Abbondanno *et al.*, Nucl. Instrum. Methods A **521**, 454 (2004).

[17] GEANT: Detector description and simulation tool, CERN Program Library W5013, 1994.

[18] S. Agostinelli *et al.*, Nucl. Instrum. Methods A **506**, 250 (2003).

[19] J. F. Briesmeister, Report LA-13709-M, Los Alamos National Laboratory, 2000.

[20] G. F. Knoll, *Radiation Detection and Measurement*, 2nd ed. (Wiley, New York, 1989), p. 120.

[21] n_TOF Collaboration, Report CERN/INTC-038, CERN, 2001.

[22] V. Vlachoudis *et al.*, in *Proceedings of the Monte Carlo 2000 Conference Lisbon, 23–26 October 2000*, edited by A. Kling, F. Barão, M. Nagakawa, L. Tavora, and P. Vaz (Springer-Verlag, Berlin, 2001).

[23] K. Wisshak, F. Voss, C. Arlandini, F. Käppeler, and L. Kazakov, Phys. Rev. C **61**, 065801 (2000).

[24] N. M. Larson, Report ORNL/TM-2000/252, Oak Ridge National Laboratory, 2000.

[25] G. Lorusso *et al.*, Nucl. Instrum. Methods A **532**, 622 (2004).

[26] K. Wisshak, K. Guber, F. Voss, F. Käppeler, and G. Reffo, Phys. Rev. C **48**, 1401 (1993).

[27] F. Fröhner, Report GA-8380, General Atomic, 1968.

[28] S. Y. Oh, J. Chang, and S. F. Mughabghab, Brookhaven Report BNL-NCS-67469, 2000.

[29] K. Wisshak, F. Voss, F. Käppeler, M. Krtička, S. Raman, A. Mengoni, and R. Gallino, Phys. Rev. C **73**, 015802 (2006).

[30] To access JEFF-3.1 data library visit the NEA Web site: www.nea.fr

[31] M. T. Pigni, H. Leeb, and the n_TOF Collaboration, ATI-NDC-2004-02.

[32] F. J. Dyson and M. L. Mehta, J. Math. Phys. **4**, 701 (1963).

[33] R. Capote, A. Ventura, F. Cannata, and J. M. Quesada, Phys. Rev. C **71**, 064320 (2005).

[34] Reference Input Parameter Library, Version 2 (RIPL-2): www-nds.iaea.org/RIPL-2/.

[35] A. Mengoni and Y. Nakajima, J. Nucl. Sci. Technol. **31**, 151 (1994).

[36] A. G. Cameron and R. M. Elkin, Can. J. Phys. **43**, 1446 (1965).

[37] E. N. Karzhavina, N. N. Fong, A. B. Popov, and A. I. Taskaev, Sov. J. Nucl. Phys. **8**, 371 (1968).

[38] N. Rosenzweig, Phys. Rev. **108**, 817 (1957).

[39] T. Rauscher, F.-K. Thielemann, and K.-L. Kratz, Phys. Rev. C **56**, 1613 (1997).

[40] A. S. Iljinov *et al.*, Nucl. Phys. **A534**, 517 (1992).

[41] F. Rahn, H. S. Camarda, G. Hacken, W. W. Havens Jr., H. I. Liou, J. Rainwater, M. Slagowitz, and S. Wynchank, Phys. Rev. C **6**, 251 (1972).

[42] H. Gruppelaar *et al.*, NEA/WPEC-17, 1998.

[43] M. Dahlfors and Y. Kadi, J. Nucl. Sci. Technol., Suppl. **2**, 1198 (2002).

[44] G. Leinweber *et al.*, Nucl. Sci. Eng. **142**, 1 (2002).

[45] Ansaldo Nucleare, EA-B0.00-1-Rev.0, 1999.

[46] A. Billebaud *et al.*, in *Proceedings of PHYSOR-2004 Topical Meeting, Chicago, 25–29 April 2004*, edited by M. Salvatores and Y. Chang (American Nuclear Society, Chicago, 2004) and references therein.

[47] F. Carminati and Y. Kadi, Report CERN/EET/Internal Note-005, CERN, 1998.

[48] Y. Kadi, Report CERN/EET/Internal Note-009, CERN, 2000.

[49] To access the ENDF/B-VI.8 database visit the Web site www.ndc.bnl.gov

[50] To access the JENDL-3.3 database visit the Web site wwwndc.tokai.jaeri.go.jp

[51] A. Herrera-Martinez, Ph.D. thesis, CERN-Thesis 2005-033, University of Cambridge, 2004.

[52] Y. Kadi and P. Revol, ICTP Lecture Notes, Vol. XII ICTP Series, edited by M. Herman, N. Paver, and A. Stanculescu, December 2002, Trieste, Italy.

[53] K. Wisshak, F. Voss, F. Käppeler, L. Kazakov, and G. Reffo, Phys. Rev. C **57**, 391 (1998).

[54] R. Reifarth *et al.*, Astrophys. J. **582**, 1251 (2003).

[55] N. Patronis *et al.*, Phys. Rev. C **69**, 025803 (2004).

[56] M. Salvatores, I. Slessarev, and A. Tchistiakov, Nucl. Sci. Eng. **130**, 309 (1998).

[57] K. Takahashi and K. Yokoi, At. Data Nucl. Data Tables **36**, 375 (1987).

[58] U. Abbondanno *et al.*, Phys. Rev. Lett. **93**, 161103 (2004).

[59] J. Best *et al.*, Phys. Rev. C **64**, 15801 (2001).

[60] R. Gallino, C. Arlandini, M. Busso, M. Lugaro, C. Travaglio, O. Straniero, A. Chieffi, and M. Limongi, Astrophys. J. **497**, 388 (1998).

[61] M. Busso, R. Gallino, and J. Wasserburg, Annu. Rev. Astron. Astrophys. **37**, 239 (1999).

[62] Z. Y. Bao, H. Beer, F. Käppeler, F. Voss, K. Whissak, and T. Rauscher, At. Data Nucl. Data Tables **76**, 70 (2000).

[63] E. Anders and N. Grevesse, Geochem. Cosmochim. Acta **53**, 197 (1989).

[64] C. Arlandini, F. Käppeler, K. Whissak, R. Gallino, M. Lugaro, M. Busso, and O. Straniero, Astrophys. J. **525**, 886 (1999).

[65] M. Rayet, M. Arnould, M. Hashimoto, N. Prantzos, and K. Nomoto, Astron. Astrophys. **298**, 517 (1995).

[66] T. Rauscher, A. Heger, R. D. Hoffman, and S. Woosley, Astrophys. J. **576**, 323 (2002).

[67] W. Aoki *et al.*, Astrophys. J. **592**, L67 (2003).

[68] C. Sneden, J. J. Cowan, J. E. Lawler, S. Burles, T. C. Beers, and G. M. Fuller, Astrophys. J. **566**, L25 (2002).

[69] C. Travaglio, R. Gallino, E. Arnone, J. Cowan, F. Jordan, and C. Sneden, Astrophys. J. **601**, 864 (2004).

[70] S. Goriely, Astron. Astrophys. **342**, 881 (1999).

[71] K. Wisshak, F. Voss, F. Käppeler, K. Guber, L. Kazakov, N. Kornilov, M. Uhl, and G. Reffo, Phys. Rev. C **52**, 2762 (1995).